

The Spatially Resolved Hot Gas Properties of NGC 1266’s AGN-Driven Outflow

SEBASTIAN LOPEZ ^{1,2}, LAURA A. LOPEZ ^{1,2}, LAURANNE LANZ ³, JUSTIN A. OTTER ⁴, AND
KATHERINE ALATALO ^{4,5}

¹*Department of Astronomy, The Ohio State University, 140 W. 18th Ave., Columbus, OH 43210, USA*

²*Center for Cosmology and AstroParticle Physics, The Ohio State University, 191 W. Woodruff Ave., Columbus, OH 43210, USA*

³*Department of Physics, The College of New Jersey, 2000 Pennington Road, Ewing, NJ 08628, USA*

⁴*William H. Miller III Department of Physics and Astronomy, Johns Hopkins University, Baltimore, MD 21218, USA*

⁵*Space Telescope Science Institute, 3700 San Martin Drive, Baltimore, MD 21218, USA*

ABSTRACT

Galactic winds play a critical role in galaxy evolution, yet their structure and driving mechanisms remain poorly understood, especially in low-luminosity AGN (LLAGN) systems. NGC 1266 hosts one such LLAGN, embedded in a massive molecular gas reservoir that is not forming stars, likely due to AGN feedback. We analyze deep archival *Chandra* data to constrain the properties of its hot gas and compare them to other wind systems. We find temperatures of 0.25 – 1.8 keV and notably high electron densities of 0.33 – 4.2 cm⁻³, suggesting significant mass loading, further supported by charge exchange emission in the southern lobe, one of the few AGN systems where it has been detected. We measure pressures and thermal energies of 10⁶ – 10⁸ K cm⁻³ and 10⁵⁴ – 10⁵⁶ erg, exceeding the minimum energy needed for the radio jet to power the outflow and implying the hot phase comprises a large fraction of the energy budget. Archival MUSE data reveal a cavity-like feature in the southern outflow, potentially associated with the far side of the outflow cone. At the maximum outflow extent, the warm and hot phases appear to be in pressure equilibrium. Coupled with short cooling timescales of ~1 Myr, comparable to the advection time, this suggests the outflow is undergoing radiative cooling and may have stalled. Finally, we compare NGC 1266 to other local AGN and starburst galaxies, finding NGC 1266 to be the densest wind in the sample.

Keywords: Early-type galaxies (429), Active galactic nuclei (16), Galactic winds (572), Shocks (2086)

1. INTRODUCTION

Galactic feedback is necessary to explain various observed properties in the Universe such as the absence of ultra-massive galaxies in cosmological simulations (Oppenheimer et al. 2010), the stellar-mass metallicity relationship (Tremonti et al. 2004), and the enrichment of the circum- and inter-galactic medium surrounding galaxies (Oppenheimer & Davé 2008). This feedback, in the form of gas outflows, or winds, and can be driven either through a starburst event like in the cases of M82 and NGC 253 (Lopez et al. 2020, 2023), or via active galactic nuclei (AGN) feedback. Regardless of origin, galactic winds are multiphase phenomenon requiring a multi-wavelength approach (X-ray, optical, radio, infrared, and ultraviolet studies) to understand the various physics occurring, such as the ejection of metal-

rich gas from the galaxy’s interstellar medium (ISM), the quenching of star formation, and stellar abundance trends in the host galaxy’s stellar disk (Veilleux et al. 2005, 2020; Thompson & Heckman 2024).

In this paper, we focus on an extreme example of AGN feedback launching tremendous outflows that stifle star formation in the galaxy NGC 1266. It is a nearby (29.9 Mpc; Cappellari et al. 2011), early-type galaxy (ETG) that has a massive CO outflow (Alatalo et al. 2011) discovered in the ATLAS^{3D} survey (Cappellari et al. 2011) and a summary of its general properties can be found in Table 1. The outflow has been studied several times in the optical and mm wavelengths: Alatalo et al. (2011) first reported the discovery of the massive molecular gas reservoir ~ 10⁹ M_⊙ as well as an outflow driving 13 M_⊙/yr from the galaxy’s ISM. Alatalo et al. (2015) later amended the estimate to 110 M_⊙/yr, assuming the outflowing gas is optically thick; the most recent ALMA observations of Otter et al. 2026 revise this downward to <85 M_⊙/yr under a multi-phase, clumpy model in which the ¹²CO traces a dif-

Table 1. Basic properties of NGC 1266.

Property	Value	Reference
R.A. (ICRS)	03 ^h 16 ^m 00 ^s .8	Gaia Collaboration (2020)
Dec. (ICRS)	−02°25′38″	Gaia Collaboration (2020)
Morphology	S0	Makarov et al. (2014)
Distance	29.9 Mpc	Cappellari et al. (2011)
Inclination	58.2°	Makarov et al. (2014)
m_B	13.8 mag	Makarov et al. (2014)
D ₂₅	1.3′	Makarov et al. (2014)
Stellar mass	$6.5 \times 10^9 M_\odot$	Leroy et al. (2019)
Black hole mass	$1.7 \times 10^6 M_\odot$	Alatalo et al. (2015)
Molecular Outflow Mass	$2.8 \times 10^8 M_\odot$	Otter et al. (2026)
Hot Gas Outflow Mass ^a	$1.35 \times 10^8 \sqrt{f} M_\odot$	This Paper
L_{FIR}	$1.3 \times 10^{10} L_\odot$	Alatalo et al. (2015)
L_X	$1.5 \times 10^7 L_\odot$	This Paper
Current SFR	$\sim 0.7 M_\odot \text{ yr}^{-1}$	Otter et al. (2024)

^a f is the filling factor of the hot gas that we assume is unity.

fuse optically thin component while dense clumps are traced by HCN(1–0). AGN-driven molecular outflows are most commonly found in luminous infrared galaxies and quasar hosts (Veilleux et al. 2020; Fluetsch et al. 2019), making NGC 1266’s outflow exceptional given its modest stellar mass and lack of merger signatures (Alatalo et al. 2011). The dearth of star formation is an indication that the outflow cannot be stellar feedback driven. Alatalo et al. (2014), using SAURON as well as UVOT, confirmed the galaxy is a post-starburst system with the youngest stellar populations confined to the central 1 kpc and current star formation constrained to the inner few hundred parsecs, indicating no large-scale star formation can drive an outflow.

The outflow in NGC 1266 must therefore be driven by an AGN. Nyland et al. (2013) used VLA and VLBA to study the radio emission of the outflow and found a high brightness temperature radio core at the center of the galaxy indicative of an AGN. Nyland et al. (2013) also found the radio emission to be consistent with other low-luminosity AGNs (LLAGNs), showing that even low-powered AGNs can drive strong outflows. Davis et al. (2012) used SAURON and GMOS IFU data to study the outflow, finding it emits in optical lines, and constrained the outflow kinematics to velocities up to 900 km s^{-1} . They also found extended low ionization emission that they attributed to shocks of the radio jet with the ambient ISM. Otter et al. (2024) studied the inner 500 pc of NGC 1266 using Gemini-NIFS and also found shocks by probing several H₂ rovibrational emission lines. These investigations, along with X-ray observations shown in Alatalo et al. (2015), demonstrate the complex, multi-phase nature of NGC 1266. In Figure 1 we show the various multiwavelength data of NGC 1266 with the HST near-infrared filters (F110W, F140W, F160W; doi:

Table 2. *Chandra* Observations Used

ObsID	Exposure	UT Start Date	Instrument
11578	30 ks	2009-09-20	ACIS-S
19498	80 ks	2016-10-10	ACIS-S
19896	40 ks	2016-10-13	ACIS-S

10.17909/wr5m-7h21) and *Chandra* X-ray data on the left, and the zoom in of the outflow on the right showing the X-ray, MUSE H α , and VLA 5 GHz radio.

Since Alatalo et al. (2015), new *Chandra* X-ray observations have been taken of NGC 1266 that, in conjunction with archival data, amount to 150 ks of data. These data now allow for a detailed analysis of the hot phase of NGC 1266’s wind and its relation to the colder phases. In this paper we conduct a spatially-resolved analysis of the X-ray spectra to constrain the temperature and volume density distributions and to make estimates of energetics of the system, comparing them to the cooler wind phases. We also take advantage of archival MUSE data to provide further insight into the ionization conditions of the wind at higher resolution than that achieved in Davis et al. (2012).

The paper is structured as follows. We describe our methodology in Section 2, and we present the hot gas properties in Section 3. We discuss the implications and compare the hot gas to other phases in Section 4. We summarize our findings in Section 5.

2. DATA & METHODS

2.1. *Chandra* X-ray Data

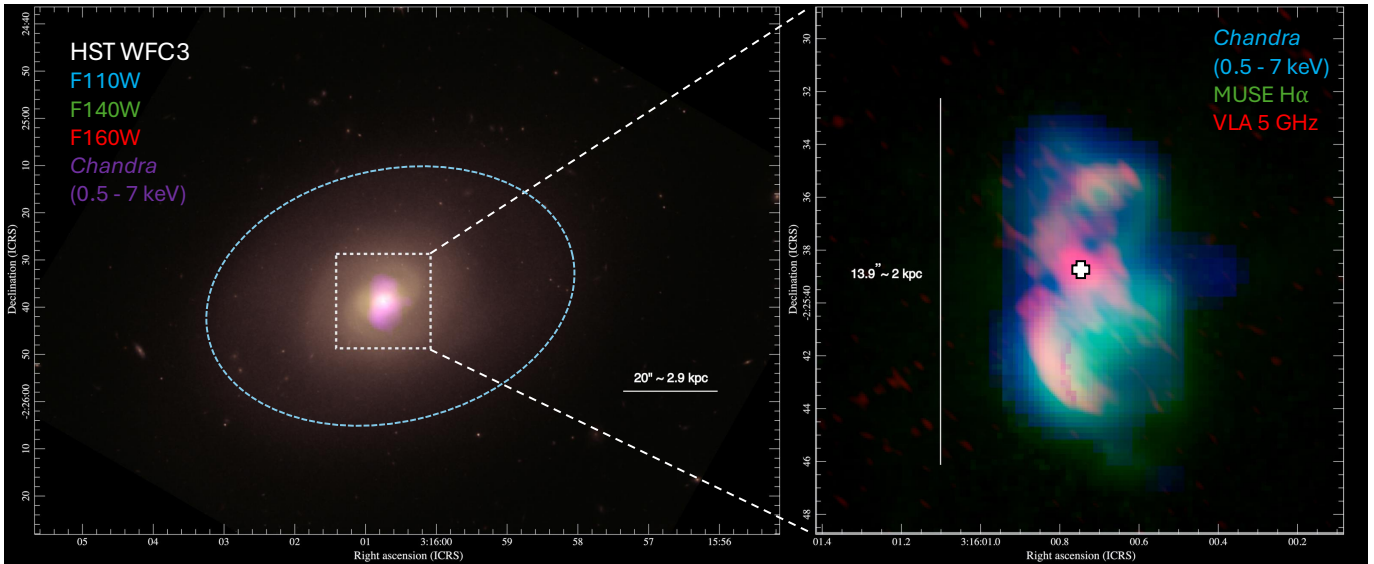


Figure 1. *Left:* Four color image of NGC 1266. The HST data show the disk in the F110W (blue), F140W (green), and F160W (red) filters while the *Chandra* X-ray data (violet) show the hot outflow. The light blue ellipse is the D_{25} isophotal diameter of $1.3'$ from Makarov et al. (2014). The white box is $20''$ by $20''$ and is the area of focus for this analysis. *Right:* Zoom-in of the white box in the left panel to highlight the multiwavelength nature of the outflow. In blue is the broad-band (0.5 – 7 keV) *Chandra* data, green is the optical $H\alpha$ data from MUSE, and red is the 5 GHz radio continuum data. The white cross marks the location of the AGN (Nyland et al. 2013). At the distance of NGC 1266 (29 Mpc; Cappellari et al. 2011), $1'$ is about 8.6 kpc.

NGC 1266 was observed three times with *Chandra* in 2009 and 2016 with ACIS-S, as detailed in Table 2 (doi: 10.25574/cdc.458). Data were downloaded from the *Chandra* archive and reduced using the Chandra Interactive Analysis of Observations CIAO version 4.15 (Fruscione et al. 2006). The observations were combined using the CIAO task *merge_obs* and then *wavdetect* was run to identify point sources that were removed using the *dmfilth* task. The resulting broad-band (0.5–7 keV) X-ray image is shown in Figure 2 along with a three-color image showing the different X-ray bandpasses of soft (0.5 – 1.2 keV), medium (1.2 – 2.0 keV), and hard (2.0 – 7.0 keV) X-rays.

To derive the hot phase properties of the outflow, we extracted the spectra from several regions along the minor axis of the galaxy. These regions are shown by the arcs in the top-left panel of Figure 2. Each region was adjusted to have at least 100 net counts to properly constrain the temperature and volume density. The center of the galaxy hosting the AGN is excluded from the data as our analysis focuses on the wind (the full AGN analysis will be in Lanz et al. in prep). Background regions were defined and subtracted from each source region. The background regions were a total area of $1.2'$ squared and located ≥ 6.4 kpc ($0.74'$) away from the galactic wind.

The spectra were extracted using the CIAO task *specextract*, and we conducted the modeling with XSPEC. We fit the spectra from each observation simultaneously. For each of the annuli shown in right panel of Figure 2, we modeled the emission as an ab-

sorbed, thermal plasma in collisional ionization equilibrium (CIE). In XSPEC, these model components were CONSTANT*TBABS*TBABS*(APEC). The constant is to account for emission variations between each observation. The two absorption components account for both the galactic absorption from the Milky Way, which we froze to $N_{\text{H}}^{\text{MW}} = 6.7 \times 10^{20} \text{ cm}^{-2}$ (HI4PI Collaboration et al. 2016) and for the intrinsic absorption of NGC 1266 (N_{H}^{1266}) which we let vary freely. Both TBABS and APEC components have their abundances set to solar, consistent with studies of post-starburst galaxies (Leung et al. 2024). Our abundances are set to those of Wilms et al. (2000), and we use the photoionization cross sections from Verner et al. (1996). We also found the annuli regions did not benefit from an added power-law continuum to the fit where the reduced χ^2 did not improve significantly statistically. We show the full the results of the annuli regions in Table 4.

We also tested for the presence of charge-exchange (CX) that has been found to make a significant portion of the total broad-band X-ray emission in various galactic wind hosts (Lopez et al. 2020, 2023; Porraz Barrera et al. 2024). CX is the process in which an ion strips an electron from a neutral atom and reflects the interaction between hot ionized and cool neutral media. We tested a composite northern region (with all the northern annuli included) and a composite southern region for CX presence using the model component ACX from Smith et al. (2012). With the added signal, we also found our regions benefited from a second APEC component. We found that the inclusion of the ACX component sta-

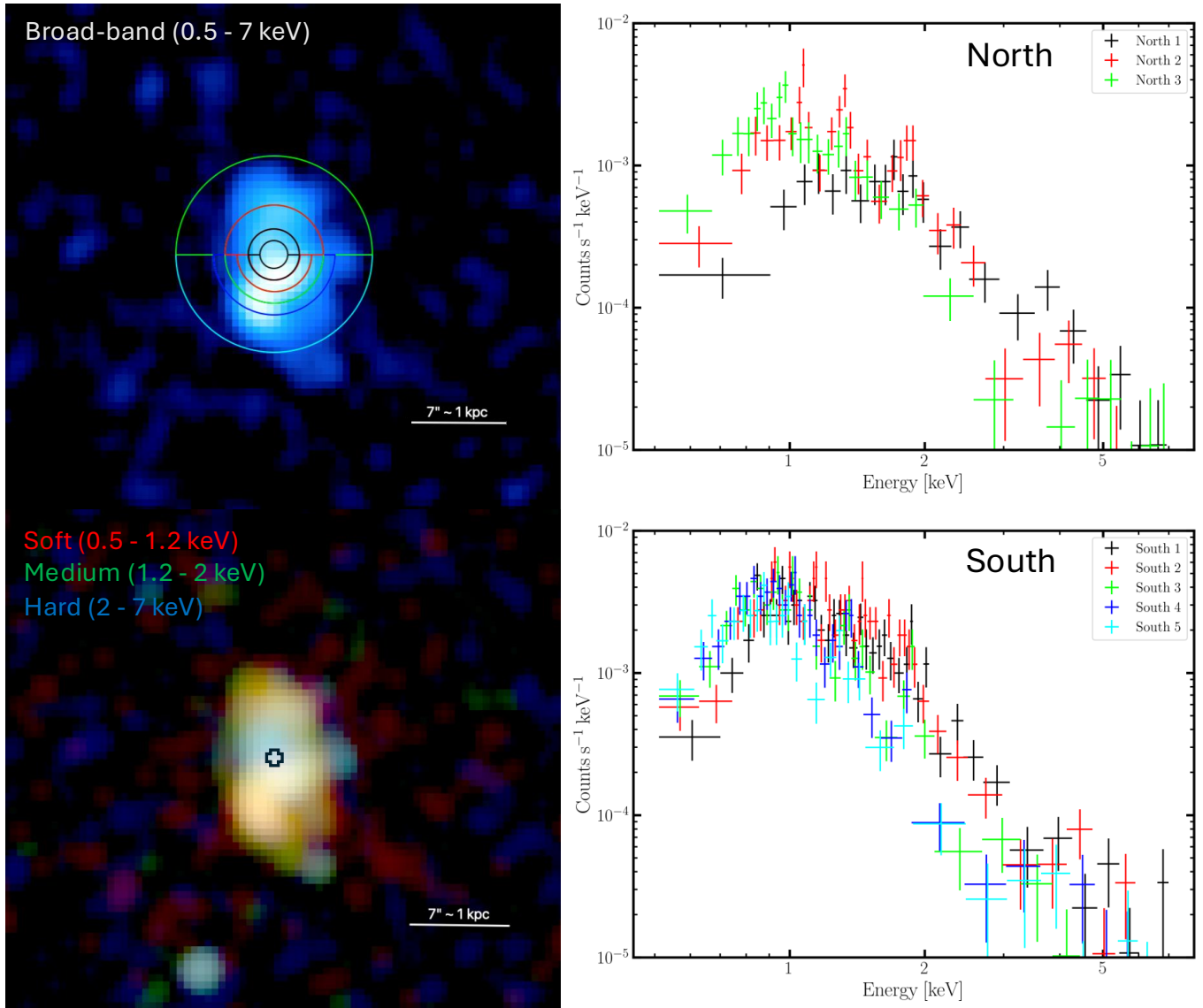


Figure 2. *Top Left:* Broad-band (0.5–7.0 keV) X-ray image of NGC 1266 overlaid with the regions used for spectral extraction. These regions span radii between one and seven arcseconds (≈ 265 – 1013 pc) and are color-coded to match the spectra shown in the right panels. At a distance of 29 Mpc, $7'' \approx 1$ kpc, as indicated by the scale bar. In these images, north is up and east is to the left. *Bottom Left:* Exposure-corrected, three-color image of NGC 1266, where red corresponds to soft (0.5–1.2 keV), green to medium (1.2–2.0 keV), and blue to hard (2.0–7.0 keV) X-ray emission. Yellow highlights soft-to-medium emission tracing the diffuse gas, while blue traces the nuclear emission as well as point sources. The AGN is marked by a cross in the three-color image. *Top Right:* The extracted and combined spectra for each of the northern annuli, colored according to their corresponding regions shown in the top left panel. *Bottom Right:* Same as the top right panel, but for the southern regions.

tistically improved the spectral fits of the southern region but not the north based on F-tests. The statistical improvement of the fits along with the full models are shown in Table 3.

In order to estimate the uncertainties on the best-fit values of Tables 3 and 4, we employ the *chain* command in XSPEC with the Goodman-Weare ensemble sampler to sample the posterior parameter space via Markov chain Monte Carlo (MCMC). We ran 40 walkers for 3×10^5 iterations and discarded the first 5×10^4 it-

erations as a burn-in to ensure the chain had converged. The reported uncertainties are 90% confidence intervals.

2.2. MUSE Optical Data

The data from the VLT’s Multi Unit Spectroscopic Explorer (MUSE) IFU instrument was acquired from the ESO Science Archive, and thus the raw data was processed by the standard MUSE pipeline (Weilbacher et al. 2020). The data covers a $1'$ by $1'$ area on the sky centered on NGC 1266 and was observed as part of

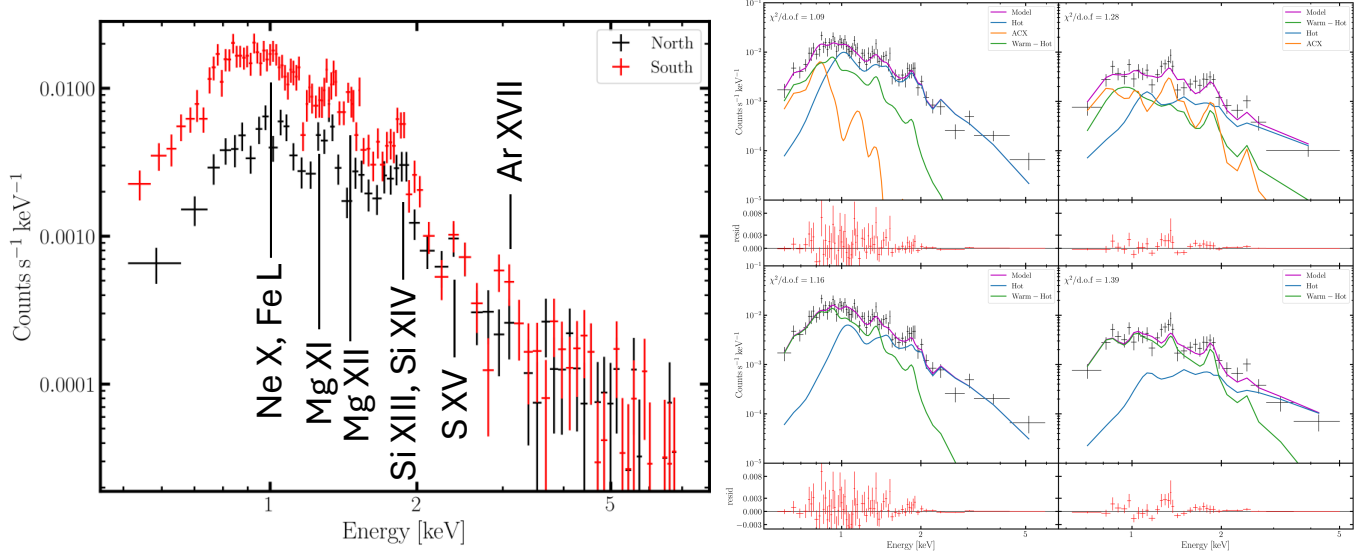


Figure 3. *Left:* Combined spectra from all three observations extracted from the northern regions and the southern regions (i.e. encompassing all the three north and five south regions in Figure 2, respectively). We label the various emission lines evident in the spectra. Spectra extracted from the composite southern region from observation 19498. *Top Middle:* The CX emission is in orange (ACX), the warm-hot thermal plasma component (APEC) is in green, and the hot thermal plasma component is in blue. The data points are in black crosses, and the residuals to the best-fit model are given below. We find that in the south, a significant portion of the broad-band X-ray emission ($\sim 38\%$) is dominated by CX emission. *Bottom Middle:* Same as the top middle panel but the model does not include CX. Without CX, the model has larger residuals at soft X-ray energies and yields a statistically worse fit. *Top Right and Bottom Right:* Same as middle panels but for the composite northern region. We do not find any improvement in the fitting when using the ACX model.

Table 3. Spectral Fits for Total North and South Regions

Region	Model ^a	N_{H} (10^{22} cm^{-2})	kT_1 (keV)	kT_2 (keV)	norm ₁ (cm^{-5})	norm ₂ (cm^{-5})	$\chi^2/\text{d.o.f}$	F-test p^b
North	APEC+APEC	$0.71^{+0.16}_{-0.10}$	$0.49^{+0.10}_{-0.18}$	$3.2^{+0.68}_{-1.2}$	$5.9^{+11}_{-2.0} \times 10^{-3}$	$1.3^{+0.71}_{-0.30} \times 10^{-3}$	84/60	
North	APEC+APEC+ACX ^c	$0.53^{+0.63}_{-0.07}$	$0.71^{+0.10}_{-0.55}$	$2.4^{+3.5}_{-1.4}$	$2.9^{+137}_{-1.6} \times 10^{-3}$	$3.5^{+7.6}_{-1.4} \times 10^{-3}$	79/59	0.06
South	APEC+APEC	$0.77^{+0.13}_{-0.09}$	$0.25^{+0.05}_{-0.03}$	$1.3^{+0.52}_{-0.16}$	$1.4^{+1.1}_{-0.53} \times 10^{-3}$	$1.13^{+0.20}_{-0.32} \times 10^{-4}$	165/142	
South	APEC+APEC+ACX	$0.85^{+0.21}_{-0.08}$	$0.22^{+0.02}_{-0.05}$	$1.1^{+0.09}_{-0.13}$	$1.1^{+3.2}_{-0.48} \times 10^{-3}$	$1.4^{+0.44}_{-0.19} \times 10^{-4}$	153/141	9.8×10^{-4}

^aAll models have a constant (CONST) component, two absorption components (TBABS), and metal abundances (Z) are set to solar (Wilms et al. 2000).

^bThe significance of the F-test p value is calculated as $1 - p$, where 3σ confidence is 0.997.

^cThe ACX component has the parameters kT , He fraction, abundance (Z), solar wind charge exchange (swcx), model, and norm. We tie the kT and Z of the ACX component to the cooler thermal plasma as that is the component expected to interact with the neutral material. The He fraction is set to the default cosmic value of 0.090909. The swcx is set to 0 as we do not expect the solar wind to contribute to the data, and model is set to 8 which is the default that sets how the code assumes electrons from the neutral participant in the CX land on the ion (Smith et al. 2012). The ACX norm values are $\text{norm}_{\text{south}} = 8.9 \times 10^{-6} \text{ cm}^{-5}$ and $\text{norm}_{\text{north}} = 3.2 \times 10^{-5} \text{ cm}^{-5}$.

program ID 0102.B-0617 (PI: A. Flütsch) on 24 January 2019 for 600 s. The data cubes covers $\lambda = 475 - 935$ nm at $R = 3026$, allowing for high resolution images (average seeing of $0.77''$) of various lines that trace electron density and temperature that will complement the X-ray data. A full optical line and kinematic analysis will be presented in future work (Otter et al. 2026 in prep.); for now we focus on the H α , H β , N II, and S II doublet to gain insight into the ionization conditions, outflow geometry, and warm phase temperature and density.

In order to measure accurate line intensities, we subtracted the stellar continuum using the PHANGS-MUSE pipeline detailed in Emsellem et al. (2022). Briefly, the pipeline runs a penalized pixel-fitting (PPXF) method from Cappellari (2017) on Voronoi-binned data using the stellar population templates from the E-MILES library Vazdekis et al. (2016). The algorithm is run multiple times to constrain the most optimal stellar kinematics, age, and metallicity to accurately model the stellar continuum being produced and allowing for it be subtracted from the cube to isolate the line emission. The continuum subtracted cube is what we use for the remainder of the analysis.

3. RESULTS

3.1. The Hot Outflow Phase

In Figure 3, we show the extracted spectra for the combined northern and southern regions of NGC 1266. Evident in the spectra are emission lines of Ne, Mg, Si, S, and Ar. We do not find the Fe K α line that is characteristically present in AGN systems since our regions did not include the central nucleus. We also notice the normalization in the <1.5 keV energy range is lower for the north than for the south despite comparable signal at >1.5 keV energies. This is an indicator of harder X-rays in the north and is evident in the three-color X-ray image in Figure 2. The lower normalization may be due to increased absorption of soft X-rays indicative of increased gas column density in the north (see Figure 4 and Table 4).

As described in the previous section, we fit absorbed thermal plasma models to the spectra from each annulus. These models are able to produce temperature kT and intrinsic column density N_{H}^{1266} which we show in the first two panels in the top left of Figure 4. Positive values of distance are of the northern outflow, and negative are along the southern outflow. We find the column densities peak in the northern outflow with $N_{\text{H}}^{1266} = (1.2_{-0.20}^{+0.26}) \times 10^{22} \text{ cm}^{-2}$ at ~ 386 pc from the center and are at their lowest, $N_{\text{H}}^{1266} = (4.7_{-1.3}^{+2.1}) \times 10^{21} \text{ cm}^{-2}$, at ~ -446 pc. We find the hot gas temperature peaks at $kT = 1.8_{-0.54}^{+2.1}$ keV or $(2.09_{-0.63}^{+2.44}) \times 10^7$ K in the first northern region 205 pc from the center, and it decreases with distance from the AGN, particularly in the southern outflow. The outflow temperatures are consistent

with those reported in Su et al. (2015) and adopted by Eskenasy et al. (2024), where $kT = 0.86 \pm 0.09$ keV.

From the thermal plasma model (APEC), the norm parameter can provide an estimate of the electron number density (n_e) as it relates to the emission measure, $\text{norm} = (10^{-14} \text{EM}) / (4\pi D^2)$, where $\text{EM} = \int n_e n_{\text{H}} dV$. Assuming $n_e = 1.2 n_{\text{H}}$, and a spherical shell geometry for each region in Figure 2, we plot the n_e in the third top panel of Figure 4. We also assume a filling factor f of unity. We find the density peaks at 205 pc with a value of high value of 4.2 cm^{-3} and decreases with distance from the AGN. We compare this value to that of other local X-ray emitting outflows in Section 4.3.

Adopting the derived values of n_e , we also calculate the cooling time of the hot gas t_{cool} , its thermal pressure P/k , and thermal energy E_{th} . The cooling time is calculated as $t_{\text{cool}} = 3kT/\Lambda n_e$, where Λ is the cooling function (with units of $\text{erg cm}^3 \text{ s}^{-1}$) for a solar plasma using PYATOMDB (Foster & Heuer 2020). We find the cooling times to be short at around 1 Myr. The thermal pressures are calculated as $P/k = 2n_e T$, peaking $\sim 10^8 \text{ K cm}^{-3}$ and decreasing with distance to $\sim 10^6 \text{ K cm}^{-3}$. As performed for the Taffy Galaxies (Appleton et al. 2015), we derived the thermal energy as $E_{\text{th}} = 3/2 n_e V kT$, where V is the spherical shell volume. We find the thermal energy to be between $E_{\text{th}} \approx 9 \times 10^{54} - 1 \times 10^{56} \text{ erg}$. These quantities are all shown in Figure 4 and listed in Table 4.

In the bottom right panel of Figure 4, we show the mass gradient of the X-ray outflow. We calculate the outflow mass as $M_{\text{out}} = n_{\text{H}} V m_{\text{H}}$, giving values ranging from $M_{\text{out}} \approx 4 \times 10^6 - 5 \times 10^7 M_{\odot}$ totaling $8.0 \times 10^7 M_{\odot}$ in the north and $5.4 \times 10^7 M_{\odot}$ in the south. To derive mass outflow rates, we use a range of outflow velocities from Davis et al. (2012), who observed ionized gas velocities near zero around the AGN up to a maximum of 900 km s^{-1} . Direct measurements of the hot gas kinematics are non-existent (though with XRISM more exceptions are being made), thus we use the optical results as a lower estimate since we expect the hot gas to exceed the warm phase in velocity (Thompson & Heckman 2024). We evaluate the mass outflow rate as $\dot{M}_X = M_{\text{out}} v_{\text{out}}/r$, where r is the projected distance of each annulus from the AGN, and sum over all annuli within the extent of the molecular outflow ($r \lesssim 460$ pc; Alatalo et al. 2011). We show these hot gas mass outflow rates in Figure 5, where we plot different gradients based on varying velocities. We find that within this region, the hot gas mass outflow rates are comparable to or exceed the molecular outflow rate: for the fastest velocity of $v_{\text{out}} = 900 \text{ km s}^{-1}$, the hot gas outflow rate exceeds the molecular gas outflow rate by a factor of 1.6, where the molecular gas estimates are from Otter et al. (2026). The minimum and maximum outflow rates of $\dot{M}_X = 61$ and $137 M_{\odot} \text{ yr}^{-1}$ correspond to velocities of $v_{\text{out}} = 400$ and 900 km s^{-1} , respectively. We note that the filling

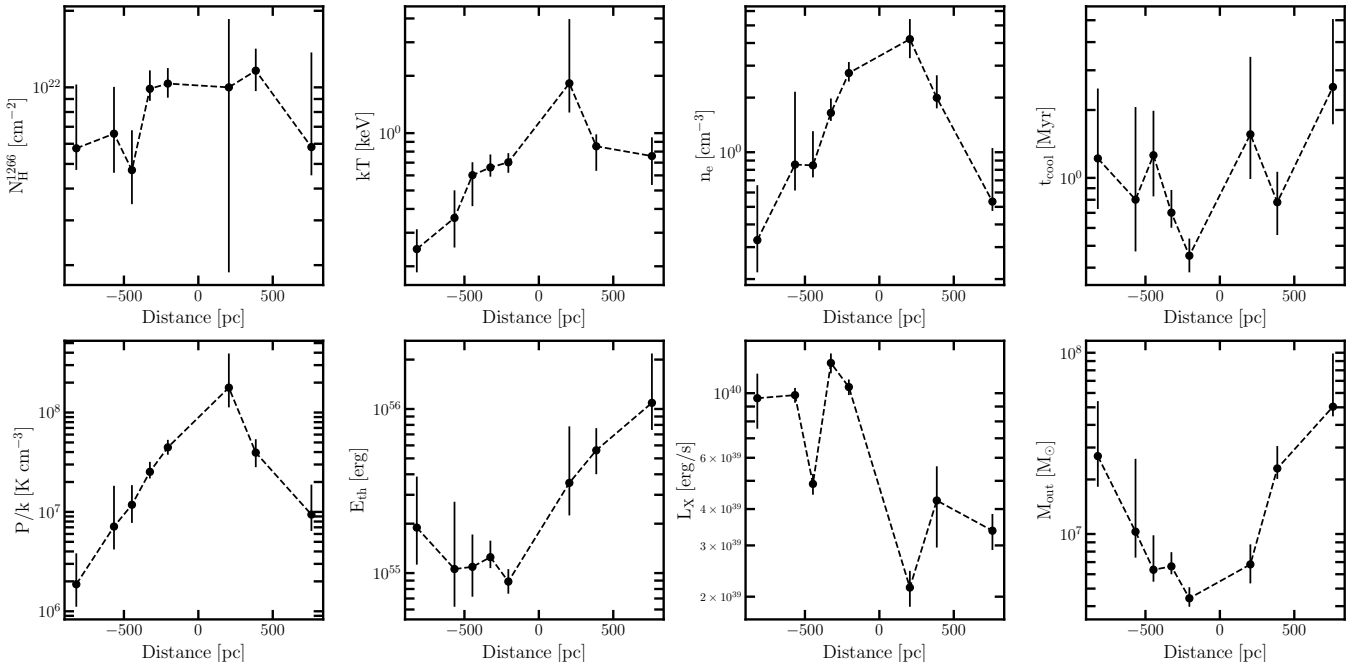


Figure 4. Gradients of measured quantities of NGC 1266’s outflow. *Top Row:* From the left to right, we plot the best-fit column density N_{H}^{1266} and temperature kT , derived electron number density n_e assuming spherical shell geometries for each region, and the hot gas cooling time t_{cool} . *Bottom Row:* From left to right, we plot the derived hot gas pressures P/k , thermal energies E_{th} , X-ray luminosities L_X , and outflow gas mass M_{out} . Positive distances are north of the center, and negative distances are south.

factor is uncertain, so these values carry a factor of $f^{1/2}$. A filling factor of $f = 0.38$ would bring the hot gas outflow mass into agreement with the molecular outflow mass at the fastest velocity. The spatial coincidence of the X-ray emission with the ionized gas outflow (Davis et al. 2012) provides the primary evidence for outward motion of the hot gas. We discuss possible interpretations of this finding, as well as our assumptions on filling factor and warm-hot phase coupling, in Section 4.1.

Using F-tests, we found that CX was statistically necessary in the southern regions but not in the north of NGC 1266. In Figure 3, we plot the spectra from observation 19498 as an example to show the model with and without a CX contribution. We find that the CX emission contributes 38% of the total luminosity, while the CIE plasma (APEC) components for the warm-hot and hot phase contribute 50% and 12%, respectively. Thus over a third of the X-ray emission of the southern lobe is a result of interactions between the hot wind and cooler surrounding medium. We note that the non-detection of CX in the north does not mean these interactions are not taking place but rather may be a result of the north pointing away from the observer as shown by the CO and ionized gas kinematics in Alatalo et al. (2011) and Davis et al. (2012), respectively. This approaching versus receding outflow asymmetry is also observed in NGC 253 (Lopez et al. 2023) and NGC 4945 (Porraz Barrera et al. 2024) where the receding outflows do not have CX detections, likely because of extinction at-

tenuating the soft X-ray emission. We also find this in Figure 3 where the north has lower emission in the soft X-ray (< 2 keV) range compared to the south.

3.2. The Warm Outflow Phase

In Figure 6, we present several optical line images, ratios, and derived quantities. All images were masked to have a signal-to-noise ratio of $\text{SNR} > 5$ using the flux error maps produced by the PHANGS-MUSE pipeline. As shown in Figure 1, the $\text{H}\alpha$ -emitting gas follows a similar morphology to the X-ray emission, with brightness enhancements in the left, south side of the outflow and in the northern, right side. Due to lower signal in the $\text{H}\beta$ map, it is less extended but nonetheless has similar features as in the $\text{H}\alpha$ image. Interestingly and more evident than in the $\text{H}\alpha$ image is a cavity-like structure to the south of the AGN location (with the latter marked by a white cross). The $\text{H}\alpha/\text{H}\beta$ ratio highlights the extremes of the two wavelengths in the middle left panel of Figure 6. The high ratio is indicative of extreme extinction and when calculating A_V using the Cardelli et al. (1989) formulation, we find values of $A_V \sim 10$, though we note that this assumes a screen-like geometry for the dust along the line of sight.

In Figure 6, we also show the sulfur doublet ratio of the 6731 Å and 6716 Å in the middle left panel that serves as a density diagnostic. Once again, we find that the cavity is evident in the line ratio and even reaches the low density limit. This is further confirmed in the bot-

Table 4. NGC 1266 Annuli Best-fit Properties

Region	Distance (pc)	N_{H} (10^{22} cm^{-2})	kT (keV)	n_e (cm^{-3})	t_{cool} (Myr)	P/k (10^7 K cm^{-3})	E_{th} (10^{55} erg)	L_X ($10^{39} \text{ erg s}^{-1}$)	M_{out} ($10^6 M_{\odot}$)	$\chi^2/\text{d.o.f}$
S5	-820	$0.58^{+0.45}_{-0.10}$	$0.25^{+0.07}_{-0.06}$	$0.33^{+0.33}_{-0.11}$	$1.2^{+1.3}_{-0.49}$	$0.19^{+0.20}_{-0.08}$	$1.9^{+2.0}_{-0.77}$	$9.6^{+2.1}_{-2.1}$	$27^{+27}_{-8.7}$	17/12
S4	-567	$0.66^{+0.35}_{-0.20}$	$0.36^{+0.14}_{-0.11}$	$0.86^{+1.3}_{-0.24}$	$0.80^{+1.3}_{-0.33}$	$0.71^{+1.1}_{-0.29}$	$1.1^{+1.7}_{-0.43}$	$9.9^{+0.57}_{-0.57}$	$10^{+16}_{-2.9}$	19/24
S3	-446	$0.47^{+0.21}_{-0.13}$	$0.60^{+0.10}_{-0.19}$	$0.85^{+0.46}_{-0.12}$	$1.3^{+0.72}_{-0.43}$	$1.2^{+0.68}_{-0.41}$	$1.1^{+0.63}_{-0.37}$	$4.9^{+0.40}_{-0.40}$	$6.4^{+3.5}_{-0.89}$	25/25
S2	-326	$0.99^{+0.18}_{-0.10}$	$0.66^{+0.11}_{-0.07}$	$1.6^{+0.33}_{-0.16}$	$0.70^{+0.18}_{-0.10}$	$2.5^{+0.66}_{-0.36}$	$1.3^{+0.33}_{-0.18}$	$13^{+0.99}_{-0.99}$	$6.6^{+1.3}_{-0.63}$	43/38
S1	-205	$1.0^{+0.16}_{-0.12}$	$0.70^{+0.08}_{-0.08}$	$2.7^{+0.41}_{-0.28}$	$0.45^{+0.09}_{-0.07}$	$4.5^{+0.85}_{-0.70}$	$0.89^{+0.17}_{-0.14}$	$11^{+0.65}_{-0.65}$	$4.4^{+0.67}_{-0.45}$	20/31
N1	205	$1.0^{+0.86}_{-0.81}$	$1.8^{+2.1}_{-0.54}$	$4.2^{+1.2}_{-0.90}$	$1.0^{+1.9}_{-0.57}$	$18^{+22}_{-6.5}$	$3.5^{+4.3}_{-1.3}$	$2.2^{+0.30}_{-0.30}$	$6.8^{+2.0}_{-1.5}$	7.4/10
N2	386	$1.2^{+0.26}_{-0.20}$	$0.85^{+0.13}_{-0.22}$	$2.0^{+0.66}_{-0.25}$	$0.78^{+0.28}_{-0.22}$	$4.0^{+1.4}_{-1.1}$	$5.6^{+2.0}_{-1.6}$	$4.3^{+1.3}_{-1.3}$	$23^{+7.6}_{-2.9}$	26/20
N4	760	$0.58^{+0.79}_{-0.13}$	$0.76^{+0.19}_{-0.22}$	$0.54^{+0.52}_{-0.06}$	$2.5^{+2.5}_{-0.80}$	$0.94^{+0.94}_{-0.30}$	$11^{+11}_{-3.5}$	$3.4^{+0.48}_{-0.48}$	$50^{+49}_{-5.8}$	26/26

tom left panel where the warm gas electron density n_e is undefined in the cavity. We derived electron densities and temperatures for each pixel using PyNeb (Luridiana et al. 2015), which simultaneously solves for n_e and T_e from the S II doublet and N II 5755 Å / 6548 + 6584 Å ratio. We find n_e values between $10 - 3000 \text{ cm}^{-3}$ and T_e values of $(0.4 - 2) \times 10^4 \text{ K}$. The resulting thermal pressures P/k are thus $4 \times 10^3 - 6 \times 10^7 \text{ K cm}^{-3}$.

In Figure 7, we plot the median n_e and P/k values from the MUSE data and their ratios with the X-ray constraints. For the MUSE data, we overlaid the same regions from the X-ray spectral extractions (as defined in Figure 2), and we took the median values from the n_e and P/k maps in each region. The n_e and P/k profiles are higher in the north than in the south though overall similar orders of magnitude, unlike the X-ray that drops more steeply with distance (Figure 4). In the ratio plots, as expected, we find the warm gas n_e values to be greater than the X-ray's by two to three orders of magnitude highlighting the more diffuse nature of the hot gas in NGC 1266. When comparing the pressures, we find that the X-ray emitting gas is overpressurized compared to the warm phase by about an order of magnitude. However, as the wind approaches the maximum observed extent of the X-ray emission ($> 700 \text{ pc}$), the two phases reach near pressure equilibrium.

4. DISCUSSION

4.1. Comparison to Previous Work

Since the discovery of NGC 1266's unusually large molecular gas reservoir in the ATLAS^{3D} (Cappellari et al. 2011) survey, numerous works have analyzed the outflow of the system across the electromagnetic spectrum. Alatalo et al. (2011) first analyzed in depth the CO data from the CARMA and SMA and discovered the molecular gas has both a highly concentrated nuclear structure and a diffuse, envelope-like extended component. The former is likely the disk that constricts the outflow, and the latter is the outflowing molecular gas it-

self, which has an average velocity of about 177 km s^{-1} . The molecular outflows extend about $R_{\text{out}} \sim 460 \text{ pc}$, which is smaller than the H α and X-ray that both go out to roughly $R_{\text{out}} \sim 1 \text{ kpc}$ (see Figure 5). According to Davis et al. (2012), this means that either the mm observations were not sensitive enough or the CO is being destroyed at these larger distances. They also noted the location of the AGN coincides with the hard X-ray emission in the *Chandra* data, which we confirm with deeper observations shown in the Figure 2.

Davis et al. (2012) studied the warm gas phase of NGC 1266's outflow using SAURON and GMOS IFU data. They found a much more rapid outflow component than the molecular gas, reaching velocities of $v_{\text{out}} \approx 900 \text{ km s}^{-1}$. These velocities are similar to the shock velocities derived by fitting the models of Allen et al. (2008) to various line ratios, indicating that the ionized gas emission is predominately or fully from shock ionization. The morphology of the optical line maps in Davis et al. (2012) match the X-ray images closely, as shown in Figure 1. This can be interpreted as the hot gas shocking the cooler ISM and producing the optical emission. As shown in Figure 3, at least in the southern lobe, over a third of the X-ray emission is a result of CX, providing additional evidence for significant hot-cool phase interactions in NGC 1266's outflow.

The GMOS images presented in Davis et al. (2012) are missing the cavity in the southern outflow apparent in the MUSE data in Figure 6. Although Davis et al. (2012) found the S II doublet ratio reaches the low density limit in several parts of the southern outflow, they did not resolve the same structure. Also studying IFU data, Eskenasy et al. (2024) analyzed MUSE images from several early-type galaxies including the same data we use for NGC 1266, and they detected the cavity-like structure. They presented the H α velocity and velocity dispersion maps, showing that the cavity is redshifted in contrast to the rest of the southern outflow that is blueshifted. If we consider the redshifted velocity struc-

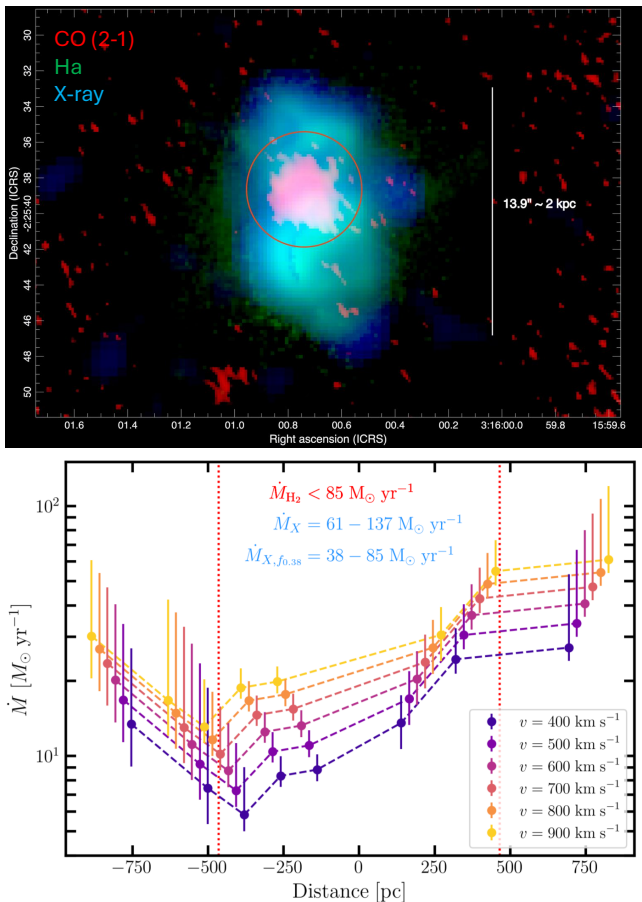


Figure 5. *Top:* Three-color image of NGC 1266 where red is the SMA CO(2-1) observations from Alatalo et al. (2011), green is VLT/MUSE H α , and blue is *Chandra* broadband X-ray emission. The red circle indicates the extent of the CO emission found in Alatalo et al. (2011), $3.23''$ or ≈ 460 pc. *Bottom:* Estimated hot gas mass outflow rates using the mass values in Table 4 and different velocities shown by the different colored lines ranging from $400 - 900$ km s $^{-1}$, the velocities of the warm gas found by Davis et al. (2012). The vertical dotted red lines show the extent of the CO(2-1) emission along with the estimated molecular gas outflow rates, the X-ray estimated outflow rates within the same region, and the X-ray outflow rates if the filling factor were low enough to keep the hot gas mass outflow rate under the molecular gas estimate as is commonly expected (Veilleux et al. 2020).

ture of the cavity along with it hitting the low density limit of S II doublet diagnostic, we surmise that the cavity is a real, astrophysical feature and potentially revealing the opposite side of the outflow cone. If this is the case, then the longer path length through the outflow, along with the dusty nature of NGC 1266’s nucleus (see the HST images in Nyland et al. 2013), would ex-

plain the high levels of extinction highlighted by the large H α /H β ratios in Figure 6.

Previous work on NGC 1266 derived the HI column densities of the outflow using 1.4 GHz continuum observations in Alatalo et al. (2011), Davis et al. (2012), and Nyland et al. (2013), and they ranged from $N_{\text{H}}^{1266} \approx (1.2 - 2.4) \times 10^{21}$ cm $^{-2}$. Alatalo et al. (2015) fit the archival *Chandra* and XMM-Newton available at the time and derive $N_{\text{H}}^{1266} = (1.5 \pm 0.2) \times 10^{21}$ cm $^{-2}$, in agreement with the 1.4 GHz continuum derived HI column densities. Our deeper *Chandra* observations find N_{H}^{1266} to range from $(4.7^{+2.1}_{-1.3}) \times 10^{21}$ to $(1.2^{+0.26}_{-0.20}) \times 10^{22}$ cm $^{-2}$, similar order of magnitude albeit slightly higher.

Lastly, and perhaps most surprisingly, we find that the hot phase outflow rates exceed the molecular gas constraints from Otter et al. (2026) assuming a maximum observed warm gas velocity of 900 km s $^{-1}$ from Davis et al. (2012). In typical galactic outflows, the cold phases dominate the mass budget (Veilleux et al. 2005, 2020). For the hot phase to exceed the cold phase in outflow rate, a few explanations should be considered. First, the outflow may be extremely mass-loaded, resulting in higher-than-typical densities. Most hot winds have $n_e \sim 0.01 - 1$ cm $^{-3}$ (see Table 5), whereas we observe peak values closer to about 4 cm $^{-3}$. The substantial charge exchange (CX) emission in the outflow may support this as it suggests the hot wind is interacting with abundant cool material and could entrain it.

Second, the mass outflow rates derived in this paper are likely overestimates. Measurements of outflow rates in edge-on systems are notoriously difficult, especially without resolved kinematics (like in the hot phase), as projection effects can bias the inferred geometry, filling factor, and luminosity, particularly due to limb-brightening along cone edges. If the filling factor is smaller than unity or the volume decreased, this would raise the implied densities and decrease the mass since $M_{\text{out}} = n_{\text{H}} m_{\text{H}} f^{1/2} V$. Thus, our estimated n_e and M_{out} are lower and upper limits, respectively. If we set the HCN values ($85 M_{\text{out}}$) as upper limits, then we find the filling factors for the hot gas to be 0.38 . Such filling factors would make the hot phase outflow rates consistent with the cool phase (albeit still unusual); however given the uncertainties, we cannot conclusively determine which considerations are more probable, and thus we note that our hot phase mass outflow rates are order-of-magnitude estimates.

4.2. What Drives the Outflow?

As mentioned earlier, Figure 7 demonstrates that the X-ray and optical emitting phases reach pressure equilibrium at the maximum extent of the outflow, ~ 750 pc. In Figure 4, we also find the cooling times are of order 1 Myr. We can estimate an advection time for the outflow as $t_{\text{adv}} = R/v_{\text{out}}$ using the velocity of Davis et al.

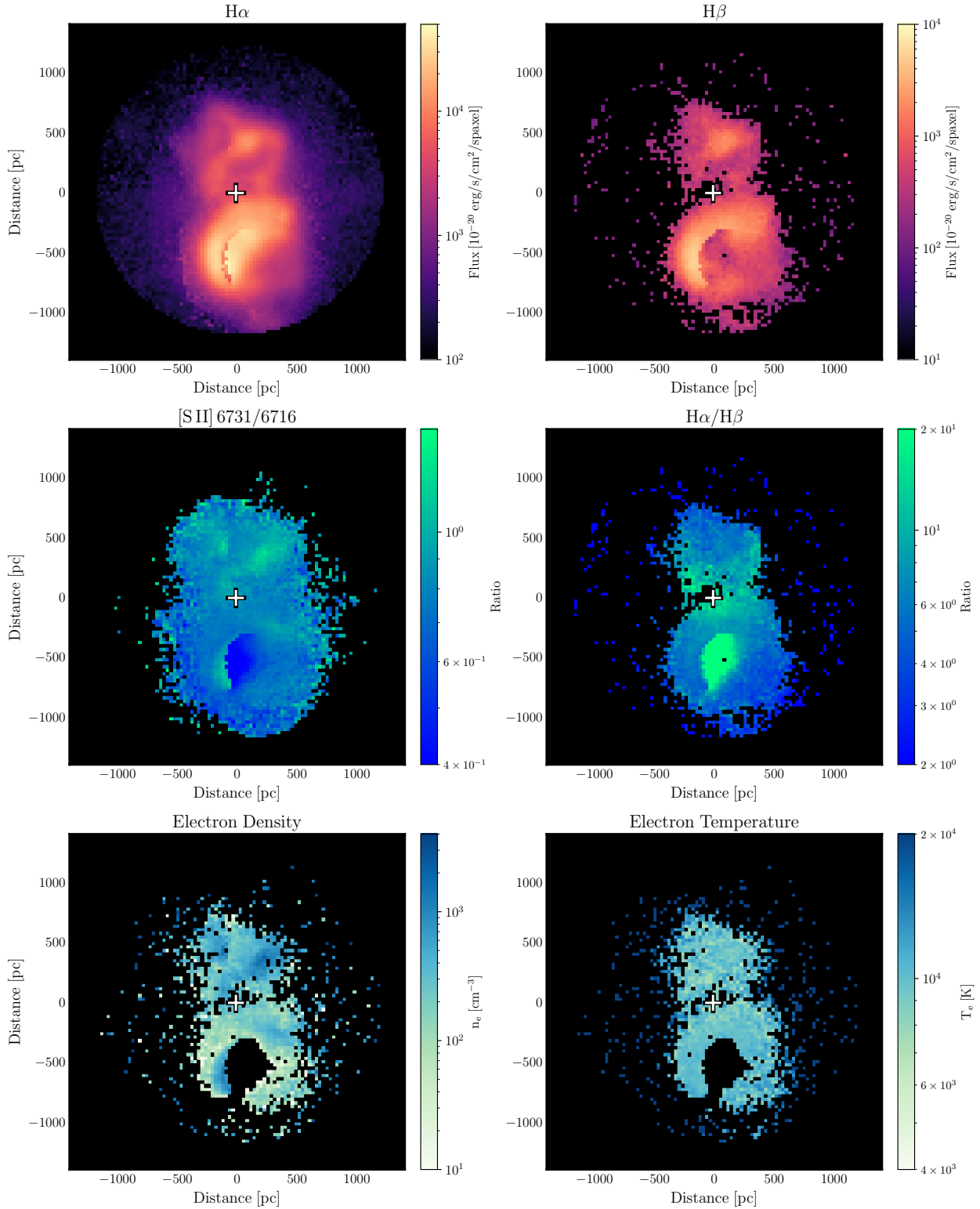


Figure 6. MUSE data products used in this paper, all of which were clipped to a signal-to-noise ratio of 5. *Top Row:* MUSE H α and H β flux maps of NGC 1266. *Middle Row:* Sulfur doublet ratio and H α /H β ratio, where the former shows it hits the low density limit in the cavity, and the latter implies heavy extinction. *Bottom Row:* Electron density n_e map from the sulfur doublet and electron temperature map T_e from the N II lines. Both values are undefined in the region of the cavity due to the low density limit.

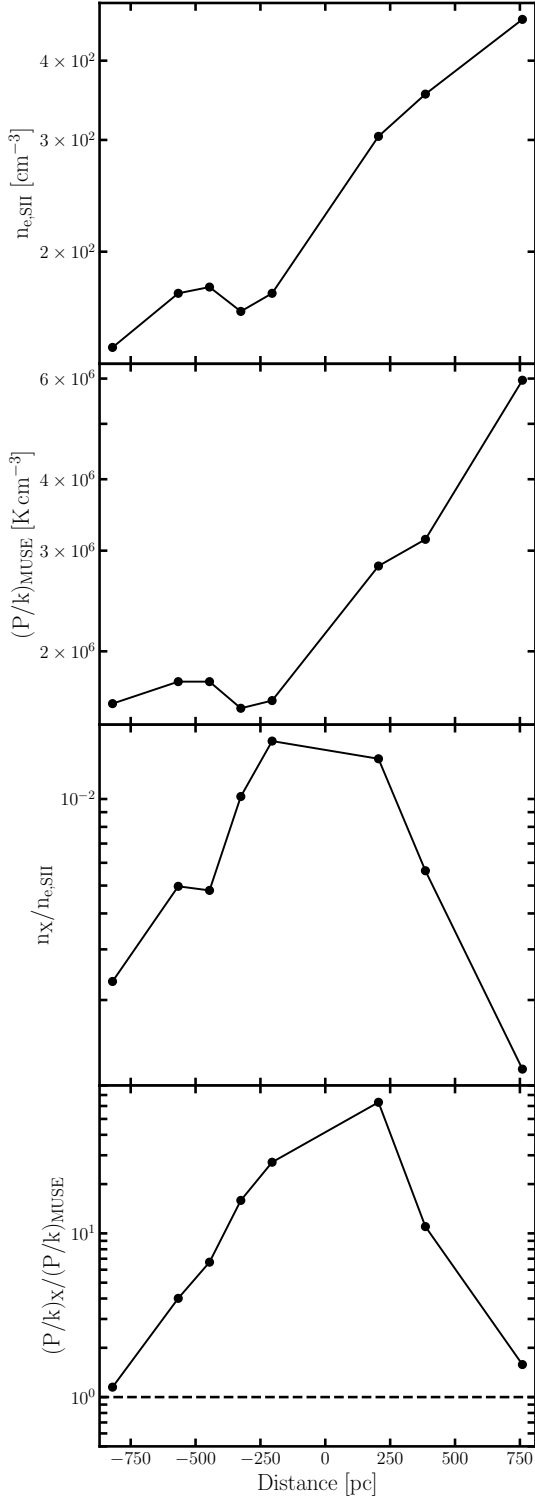


Figure 7. *First and Second:* Gradients with distance of the median n_e and P/k values from the MUSE data. *Third and Fourth:* Ratio plots comparing the n_e and P/k values from MUSE and our X-ray spectral analysis. We find that the warm and hot outflow phases reach near pressure equilibrium at the outflows maximum extent.

(2012) of $v_{\text{out}} = 900 \text{ km s}^{-1}$ and the maximum outflow extent of $R \approx 1 \text{ kpc}$. We find that the advection time is $t_{\text{adv}} \approx 1.1 \text{ Myr}$, comparable to the cooling times, suggesting that the outflow is likely undergoing bulk radiative cooling (Wang 1995; Thompson et al. 2016). This finding implies that the hot wind, barring future AGN episodes, is no longer able to maintain a strong pressure gradient to drive further expansion. Instead, it may be entering a mechanically-exhausted phase in which the outflow stalls and the hot gas begins to cool and mix with the surrounding medium, potentially explaining the close $\text{H}\alpha$ correspondence (Eskenasy et al. 2024). We do exercise caution here with this interpretation as the uncertainties with the volume and filling factor may result in the densities being underestimated. If that is the case, then the X-ray derived pressures would increase above pressure equilibrium, thereby continuing the outflow episode.

Whether or not the outflow has stalled, the origin of the energy driving it remains uncertain. The physical picture is that the radio jet, which Nyland et al. (2013) show is deeply embedded within the dense nuclear molecular gas reservoir, inflates a cocoon of hot plasma that drives a forward shock into the surrounding ISM (Wagner et al. 2012; Mukherjee et al. 2016). This overpressured hot cocoon acts as the primary intermediary between the jet and the cold molecular gas, driving the bulk of the molecular outflow as it expands. In this frustrated jet scenario (Mukherjee et al. 2016), where the jet remains confined on sub-kpc scales, the coupling is particularly efficient as essentially all of the jet energy is deposited locally rather than escaping to larger scales. Nyland et al. (2013) found that the minimum jet energy is about $1.7 \times 10^{54} \text{ erg}$, which is an order of magnitude lower than the kinetic molecular energy estimated by Alatalo et al. (2011) at 10^{55} erg . The former argues that since the true energy of the radio lobes may be higher than the minimum estimate, it is feasible that the lobes are capable of driving the outflow. In Figure 4, we show the thermal energy distribution across the outflow, finding values that range from $\sim 10^{55} - 10^{56} \text{ erg}$. Our results indicate that the hot, X-ray-emitting phase contains a substantial fraction of the total energy budget of the outflow. If the true jet energy exceeds the minimum estimate from Nyland et al. (2013), then the observed thermal energy in the hot phase implies that a non-negligible fraction of the jet’s power must have been deposited into the surrounding ISM. While the exact coupling efficiency remains uncertain due to the unknown total jet energy, the hot gas carries a substantial portion of the outflow energy budget in both thermal and kinetic form. The thermal energy of the hot phase ranges from $\sim 10^{55} - 10^{56} \text{ erg}$, while the kinetic energy $E_{\text{kin}} = \frac{1}{2} M_X v_{\text{out}}^2 \sim 10^{56} - 10^{57} f^{1/2} \text{ erg}$ for $v_{\text{out}} = 400 - 900 \text{ km s}^{-1}$, comparable to or exceeding the thermal energy at higher velocities and comparable to the molec-

ular outflow kinetic energy of 10^{55} erg (Alatalo et al. 2011).

4.3. Comparison to other wind hosts

Compared to other X-ray emitting wind hosts, NGC 1266 sits in a unique position, particularly due to its high density. We note that comparing n_e across different systems can introduce uncertainties due to differing volumes. To best compare to other AGN radio jet driven systems, we rederive the properties for NGC 1266 for the total southern and northern outflows using the spectral models in Table 3. For comparison, we also include starburst-driven winds (Lopez et al. 2020, 2023; Porraz Barrera et al. 2024). We compile the values in Table 5, including the re-derived integrated properties of the northern and southern outflow lobes of NGC 1266. The comparison sample was selected to include all available galaxies with spatially resolved X-ray spectroscopic measurements of outflowing gas in the literature, spanning both AGN jet-driven and starburst-driven winds, reflecting the currently limited number of such studies.

First, we compare our total outflow shell results for NGC 1266 to previous *Chandra* X-ray derived properties of AGN hosts: M84 (Bambic et al. 2023), NGC 3801 (Croston et al. 2007), NGC 6764 (Croston et al. 2008), the Circinus Galaxy (Mingo et al. 2012), and Mrk 573 (Paggi et al. 2012). We find that NGC 1266, even after calculating n_e for a larger volume, still has n_e values two orders of magnitude greater than NGC 3801 and Circinus. Meanwhile with M84, Mrk 573, and NGC 6764, the n_e values are similar, though NGC 1266 is still on the higher end of the ranges. The temperatures are all roughly consistent, as expected of the hot wind phase. For NGC 3801, NGC 6764, and Circinus, the total thermal energies span the range of $0.5 - 5 \times 10^{55}$ erg, also roughly consistent with NGC 1266. Thus in this small sample, NGC 1266 is similarly energetic to other AGN though above average in hot wind densities. More follow-up work is needed with larger samples to truly understand where NGC 1266 lies compared to other AGN outflows.

While NGC 1266 is not a starburst (Nyland et al. 2013) as its star formation rate is too low to drive a wind (Otter et al. 2024), we still compare the outflow to other previous edge-on, spatially-resolved X-ray analysis of starburst wind hosts: M82 (Lopez et al. 2020), NGC 253 (Lopez et al. 2023), and NGC 4945 (Porraz Barrera et al. 2024). For these sources, the spectra were modeled for smaller regions as opposed to the total lobes as is done for the AGN studies. As a result, the values shown in brackets in Table 5 are most comparable between NGC 1266 and the starbursts. We find the values for NGC 1266 to be well within the range of the starburst galaxies except for n_e in the inner ± 325 that exceeds the starbursts. This highlights the incredibly dense nature of NGC 1266's wind likely due to its massive molecu-

lar gas reservoir being entrained by the hot phase and creating the CX emission.

4.4. Charge Exchange Detection

Previous work has shown that charge exchange (CX), the stripping of an electron from a neutral atom by an ion, can be a prominent feature in X-ray emission, though much of the work has been for star-forming systems rather than AGN. For example, Liu et al. (2012) showed that the $K\alpha$ triplet of He-like ions required a CX component to account for the observed line ratios for several nearby star-forming galaxies. The recent works of Lopez et al. (2020), Lopez et al. (2023), and Porraz Barrera et al. (2024) also found significant CX contributions ($\sim 12-42\%$) to broad-band *Chandra* spectra in M82, NGC 253, and NGC 4945.

CX analyses for AGN-driven outflows are scarce, though one example is the work of Yang et al. (2020) who analyzed XMM-Newton RGS spectra of M51's central region. They found that most of the soft X-ray emission originates from the AGN outflow and its interactions with the neutral material surrounding it. Due to the observations using X-ray gratings, they had high spectral resolution to observe directly the prominent O VII forbidden lines that are enhanced with CX. They found that CX makes up a significant fraction of the diffuse X-ray emission, about 21%. The robust result of Yang et al. (2020) indicates that AGN-driven outflows, like the starburst ones, are able to produce CX emission as long as neutral material is interacting with hot gas, as is the case in NGC 1266. Unfortunately, high resolution X-ray spectra of NGC 1266, particularly of the O VII forbidden lines, are not available, so future observations are merited to better quantify the CX contribution. Moreover, the detection of CX in both M51 and NGC 1266 provides a case for revisiting the AGN outflow studies listed in Table 5 to test for CX emission.

5. CONCLUSION

We analyze 150 ks of archival *Chandra* data to constrain the hot phase properties of NGC 1266 as well as derive warm gas electron number densities and temperatures from archival MUSE data. We summarize our results as follows:

- We find temperatures between 0.25 and 1.8 keV peaking near the center of NGC 1266. We derive high electron number densities uncommon in starburst and AGN-driven galactic winds, ranging from $0.33 - 4.2 \text{ cm}^{-3}$. Assuming a filling factor of one, these densities imply high mass outflow rates and short cooling times of order 1 Myr, indicative of the outflows undergoing rapid radiative cooling. The derived outflow rates are in excess of the cold molecular constraints from the literature, and this discrepancy can be resolved if the filling factor is less than unity, but that would lead to even greater electron densities.

Table 5. Outflow Properties of Comparison Galaxies

Galaxy	Type	kT [keV]	n_e [cm^{-3}]	P/k [$\times 10^6$ K cm^{-3}]	Reference
NGC 1266 ^a	AGN	0.23 – 0.77 [0.24 – 1.8]	0.24 – 0.73 [0.33 – 4.2]	1.9 – 11 [1.9 – 180]	This Paper
M84	AGN	0.5 – 0.9	0.1 – 0.5	6 – 20	Bambic et al. (2023)
NGC 3801	AGN	0.2 – 1.0	0.01 – 0.03	0.04 – 1.2	Croston et al. (2007)
NGC 6764	AGN	0.6 – 0.8	0.2 – 0.3	4.2 – 8.4	Croston et al. (2008)
Circinus	AGN	0.7 – 1.8	0.02	0.8 – 1.4	Mingo et al. (2012)
Mrk 573	AGN	0.76 – 1.29	0.14 – 0.52	2.75 – 16.9	Paggi et al. (2012)
M82	SB	0.4 – 3.4	0.04 – 1.8	0.6 – 212	Lopez et al. (2020), Nguyen & Thompson (2021)
NGC 253	SB	0.2 – 0.9	0.1 – 2	0.8 – 62	Lopez et al. (2023)
NGC 4945	SB	0.1 – 1	0.04 – 1.7	0.2 – 42	Porraz Barrera et al. (2024)

^aValues listed for NGC 1266 are for the southern and northern lobe to best compare to previous AGN studies that use similar geometry. Since these values have two temperature components, we take the flux weighted average for each component and report it in the table. The values in brackets are the values from Figure 4. Compared to the rest of the sample, we find that NGC 1266 either sits at the high end of ranges or is a factor of a few denser than other X-ray emitting winds.

- When considering the spectra from the whole northern and southern outflows, we find that charge-exchange (CX) statistically improves the spectral fitting of the southern lobe but not of the northern lobe. The CX emission makes up over a third of the total broad-band X-ray emission in the southern outflow, implying abundant interactions between the hot phase and neutral ISM. Along with M51 (Yang et al. 2020), NGC 1266 is one of the few AGN systems where CX has been detected to date.
- We constrain the thermal energy of the outflow to be in the range of $10^{54} - 10^{56}$ erg. This is in excess of the previous minimum jet energy of 1.7×10^{54} erg (Nyland et al. 2013). Thus, regardless of whether the radio jet solely drives the outflow, the hot phase composes a large fraction of the energy budget.
- We reprocess the MUSE data for NGC 1266 using the PHANGS-MUSE pipeline (Emsellem et al. 2022). We find a cavity-like feature in the southern outflow most evident in the $H\beta$ map. The ratio of $H\alpha/H\beta$ is in excess of 10 in the cavity, implying heavy extinction. The S II doublet ratio also reaches the low-density limit in the cavity, implying very diffuse material is present. Based on the kinematic map of (Eskenasy et al. 2024), we hypothesize that the cavity is the receding side of the outflow; however a full kinematic analysis in future work (Otter et al. 2026 in prep) is necessary to determine its origin.
- We find spatial agreement between the X-ray and $H\alpha$ images, the latter of which has been shown to originate from shocks. Thus it is likely the hot wind is shocking the ambient medium and producing the $H\alpha$. We find that the X-ray emitting gas is over-pressurized compared to the warm gas in the inner wind, but the two phases approach pressure equilibrium at the maximum wind extent of ~ 750 pc indicating the wind may stall there barring future AGN activity.
- We compare our results to other nearby AGN and starburst systems. We find that while the thermal energies are similar between NGC 1266 and other AGN, NGC 1266's hot wind is denser by a factor of a few. When comparing with starbursts, we find NGC 1266 is also denser though only near the AGN and is similar in density past 325 pc.

Software: CIAO (v4.15; Fruscione et al. 2006), XSPEC (v12.13.0c; Arnaud 1996)

ACKNOWLEDGMENTS

SL and LAL were supported by NASA's Astrophysics Data Analysis Program under grant No. 80NSSC22K0496SL, and LAL also acknowledges support through the Heising-Simons Foundation grant 2022-3533. SL and LAL also thank the OSU Galaxy/ISM Meeting for useful discussions and Tim Davis for helpful feedback on the optical line data anal-

yses. We also acknowledge the usage of the HyperLeda database <http://leda.univ-lyon1.fr>

ACKNOWLEDGMENTS

REFERENCES

- Alatalo, K., Blitz, L., Young, L. M., et al. 2011, *ApJ*, 735, 88, doi: [10.1088/0004-637X/735/2/88](https://doi.org/10.1088/0004-637X/735/2/88)
- Alatalo, K., Nyland, K., Graves, G., et al. 2014, *ApJ*, 780, 186, doi: [10.1088/0004-637X/780/2/186](https://doi.org/10.1088/0004-637X/780/2/186)
- Alatalo, K., Lacy, M., Lanz, L., et al. 2015, *ApJ*, 798, 31, doi: [10.1088/0004-637X/798/1/31](https://doi.org/10.1088/0004-637X/798/1/31)
- Allen, M. G., Groves, B. A., Dopita, M. A., Sutherland, R. S., & Kewley, L. J. 2008, *ApJS*, 178, 20, doi: [10.1086/589652](https://doi.org/10.1086/589652)
- Appleton, P. N., Lanz, L., Bitsakis, T., et al. 2015, *ApJ*, 812, 118, doi: [10.1088/0004-637X/812/2/118](https://doi.org/10.1088/0004-637X/812/2/118)
- Arnaud, K. A. 1996, in *Astronomical Society of the Pacific Conference Series*, Vol. 101, *Astronomical Data Analysis Software and Systems V*, ed. G. H. Jacoby & J. Barnes, 17
- Bambic, C. J., Russell, H. R., Reynolds, C. S., et al. 2023, *MNRAS*, 522, 4374, doi: [10.1093/mnras/stad824](https://doi.org/10.1093/mnras/stad824)
- Cappellari, M. 2017, *MNRAS*, 466, 798, doi: [10.1093/mnras/stw3020](https://doi.org/10.1093/mnras/stw3020)
- Cappellari, M., Emsellem, E., Krajnović, D., et al. 2011, *MNRAS*, 413, 813, doi: [10.1111/j.1365-2966.2010.18174.x](https://doi.org/10.1111/j.1365-2966.2010.18174.x)
- Cardelli, J. A., Clayton, G. C., & Mathis, J. S. 1989, *ApJ*, 345, 245, doi: [10.1086/167900](https://doi.org/10.1086/167900)
- Croston, J. H., Hardcastle, M. J., Kharb, P., Kraft, R. P., & Hota, A. 2008, *ApJ*, 688, 190, doi: [10.1086/592268](https://doi.org/10.1086/592268)
- Croston, J. H., Kraft, R. P., & Hardcastle, M. J. 2007, *ApJ*, 660, 191, doi: [10.1086/513500](https://doi.org/10.1086/513500)
- Davis, T. A., Krajnović, D., McDermid, R. M., et al. 2012, *MNRAS*, 426, 1574, doi: [10.1111/j.1365-2966.2012.21770.x](https://doi.org/10.1111/j.1365-2966.2012.21770.x)
- Emsellem, E., Schinnerer, E., Santoro, F., et al. 2022, *A&A*, 659, A191, doi: [10.1051/0004-6361/202141727](https://doi.org/10.1051/0004-6361/202141727)
- Eskenasy, R., Olivares, V., Su, Y., & Li, Y. 2024, *MNRAS*, 527, 1317, doi: [10.1093/mnras/stad3209](https://doi.org/10.1093/mnras/stad3209)
- Fluetsch, A., Maiolino, R., Carniani, S., et al. 2019, *MNRAS*, 483, 4586, doi: [10.1093/mnras/sty3449](https://doi.org/10.1093/mnras/sty3449)
- Foster, A. R., & Heuer, K. 2020, *Atoms*, 8, 49, doi: [10.3390/atoms8030049](https://doi.org/10.3390/atoms8030049)
- Fruscione, A., McDowell, J. C., Allen, G. E., et al. 2006, in *Society of Photo-Optical Instrumentation Engineers (SPIE) Conference Series*, Vol. 6270, *Society of Photo-Optical Instrumentation Engineers (SPIE) Conference Series*, ed. D. R. Silva & R. E. Doxsey, 62701V, doi: [10.1117/12.671760](https://doi.org/10.1117/12.671760)
- Gaia Collaboration. 2020, *VizieR Online Data Catalog: Gaia EDR3 (Gaia Collaboration, 2020)*, *VizieR On-line Data Catalog: I/350*. Originally published in: 2021A&A...649A...1G, doi: [10.26093/cds/vizieR.1350](https://doi.org/10.26093/cds/vizieR.1350)
- HI4PI Collaboration, Ben Bekhti, N., Flöer, L., et al. 2016, *A&A*, 594, A116, doi: [10.1051/0004-6361/201629178](https://doi.org/10.1051/0004-6361/201629178)
- Leroy, A. K., Sandstrom, K. M., Lang, D., et al. 2019, *ApJS*, 244, 24, doi: [10.3847/1538-4365/ab3925](https://doi.org/10.3847/1538-4365/ab3925)
- Leung, H.-H., Wild, V., Papatthomas, M., et al. 2024, *MNRAS*, 528, 4029, doi: [10.1093/mnras/stae225](https://doi.org/10.1093/mnras/stae225)
- Liu, J., Wang, Q. D., & Mao, S. 2012, *MNRAS*, 420, 3389, doi: [10.1111/j.1365-2966.2011.20263.x](https://doi.org/10.1111/j.1365-2966.2011.20263.x)
- Lopez, L. A., Mathur, S., Nguyen, D. D., Thompson, T. A., & Olivier, G. M. 2020, *ApJ*, 904, 152, doi: [10.3847/1538-4357/abc010](https://doi.org/10.3847/1538-4357/abc010)
- Lopez, S., Lopez, L. A., Nguyen, D. D., et al. 2023, *ApJ*, 942, 108, doi: [10.3847/1538-4357/aca65e](https://doi.org/10.3847/1538-4357/aca65e)
- Luridiana, V., Morisset, C., & Shaw, R. A. 2015, *A&A*, 573, A42, doi: [10.1051/0004-6361/201323152](https://doi.org/10.1051/0004-6361/201323152)
- Makarov, D., Prugniel, P., Terekhova, N., Courtois, H., & Vauglin, I. 2014, *A&A*, 570, A13, doi: [10.1051/0004-6361/201423496](https://doi.org/10.1051/0004-6361/201423496)
- Mingo, B., Hardcastle, M. J., Croston, J. H., et al. 2012, *ApJ*, 758, 95, doi: [10.1088/0004-637X/758/2/95](https://doi.org/10.1088/0004-637X/758/2/95)
- Mukherjee, D., Bicknell, G. V., Sutherland, R., & Wagner, A. 2016, *MNRAS*, 461, 967, doi: [10.1093/mnras/stw1368](https://doi.org/10.1093/mnras/stw1368)
- Nguyen, D. D., & Thompson, T. A. 2021, *MNRAS*, 508, 5310, doi: [10.1093/mnras/stab2910](https://doi.org/10.1093/mnras/stab2910)
- Nyland, K., Alatalo, K., Wrobel, J. M., et al. 2013, *ApJ*, 779, 173, doi: [10.1088/0004-637X/779/2/173](https://doi.org/10.1088/0004-637X/779/2/173)
- Oppenheimer, B. D., & Davé, R. 2008, *MNRAS*, 387, 577, doi: [10.1111/j.1365-2966.2008.13280.x](https://doi.org/10.1111/j.1365-2966.2008.13280.x)
- Oppenheimer, B. D., Davé, R., Kereš, D., et al. 2010, *MNRAS*, 406, 2325, doi: [10.1111/j.1365-2966.2010.16872.x](https://doi.org/10.1111/j.1365-2966.2010.16872.x)

- Otter, J. A., Alatalo, K., Rowlands, K., et al. 2024, *ApJ*, 975, 142, doi: [10.3847/1538-4357/ad793a](https://doi.org/10.3847/1538-4357/ad793a)
- . 2026, *ApJ*, 997, 361, doi: [10.3847/1538-4357/ae2c5a](https://doi.org/10.3847/1538-4357/ae2c5a)
- Paggi, A., Wang, J., Fabbiano, G., Elvis, M., & Karovska, M. 2012, *ApJ*, 756, 39, doi: [10.1088/0004-637X/756/1/39](https://doi.org/10.1088/0004-637X/756/1/39)
- Porraz Barrera, N., Lopez, S., Lopez, L. A., et al. 2024, *ApJ*, 968, 54, doi: [10.3847/1538-4357/ad4606](https://doi.org/10.3847/1538-4357/ad4606)
- Smith, R. K., Foster, A. R., & Brickhouse, N. S. 2012, *Astronomische Nachrichten*, 333, 301, doi: [10.1002/asna.201211673](https://doi.org/10.1002/asna.201211673)
- Su, Y., Irwin, J. A., White, III, R. E., & Cooper, M. C. 2015, *ApJ*, 806, 156, doi: [10.1088/0004-637X/806/2/156](https://doi.org/10.1088/0004-637X/806/2/156)
- Thompson, T. A., & Heckman, T. M. 2024, *ARA&A*, 62, 529, doi: [10.1146/annurev-astro-041224-011924](https://doi.org/10.1146/annurev-astro-041224-011924)
- Thompson, T. A., Quataert, E., Zhang, D., & Weinberg, D. H. 2016, *MNRAS*, 455, 1830, doi: [10.1093/mnras/stv2428](https://doi.org/10.1093/mnras/stv2428)
- Tremonti, C. A., Heckman, T. M., Kauffmann, G., et al. 2004, *ApJ*, 613, 898, doi: [10.1086/423264](https://doi.org/10.1086/423264)
- Vazdekis, A., Koleva, M., Ricciardelli, E., Röck, B., & Falcón-Barroso, J. 2016, *MNRAS*, 463, 3409, doi: [10.1093/mnras/stw2231](https://doi.org/10.1093/mnras/stw2231)
- Veilleux, S., Cecil, G., & Bland-Hawthorn, J. 2005, *ARA&A*, 43, 769, doi: [10.1146/annurev.astro.43.072103.150610](https://doi.org/10.1146/annurev.astro.43.072103.150610)
- Veilleux, S., Maiolino, R., Bolatto, A. D., & Aalto, S. 2020, *A&A Rv*, 28, 2, doi: [10.1007/s00159-019-0121-9](https://doi.org/10.1007/s00159-019-0121-9)
- Verner, D. A., Ferland, G. J., Korista, K. T., & Yakovlev, D. G. 1996, *ApJ*, 465, 487, doi: [10.1086/177435](https://doi.org/10.1086/177435)
- Wagner, A. Y., Bicknell, G. V., & Umemura, M. 2012, *ApJ*, 757, 136, doi: [10.1088/0004-637X/757/2/136](https://doi.org/10.1088/0004-637X/757/2/136)
- Wang, B. 1995, *ApJ*, 444, 590, doi: [10.1086/175633](https://doi.org/10.1086/175633)
- Weilbacher, P. M., Palsa, R., Streicher, O., et al. 2020, *A&A*, 641, A28, doi: [10.1051/0004-6361/202037855](https://doi.org/10.1051/0004-6361/202037855)
- Wilms, J., Allen, A., & McCray, R. 2000, *ApJ*, 542, 914, doi: [10.1086/317016](https://doi.org/10.1086/317016)
- Yang, H., Zhang, S., & Ji, L. 2020, *ApJ*, 894, 22, doi: [10.3847/1538-4357/ab80c9](https://doi.org/10.3847/1538-4357/ab80c9)